

One loop effects of natural SUSY in third generation fermion production at the ILC

Yusaku Kouda^{1,*}, Tadashi Kon¹, Yoshimasa Kurihara², Tadashi Ishikawa²,
Masato Jimbo³, Kiyoshi Kato⁴ and Masaaki Kuroda⁵

¹ Seikei University, Musashino, Tokyo 180-8633, Japan

* E-mail: dd146101@cc.seikei.ac.jp

² KEK, Tsukuba, Ibaraki 305-0801, Japan

³ Chiba University of Commerce, Ichikawa, Chiba 272-0827, Japan

⁴ Kogakuin University, Shinjuku, Tokyo 163-8677, Japan

⁵ Meiji Gakuin University, Yokohama, Kanagawa 244-8539, Japan

Abstract

We investigate the 1-loop effects of supersymmetric particles on the third-generation fermion-pair production at the ILC within the framework of the Minimal Supersymmetric Standard Model. Three sets of the SUSY parameters are proposed which are consistent with the observed Higgs mass, the muon $g-2$, the Dark Matter abundance, etc. We discuss on the possibility of discovering the signals consistent with SUSY as well as of experimentally distinguishing the proposed sets of SUSY parameters.

1 Introduction

The Large Hadron Collider (LHC) has completed its first run and succeeded spectacularly by discovering the Higgs particle with a mass about 126 GeV[1, 2]. This discovery has marked a landslide victory of the standard model (SM). In order to explain the elementary scalar Higgs with a mass $\mathcal{O}(10^2)$ GeV in the framework of the Grand Unified Theory (GUT), we consider the minimal supersymmetric (SUSY) extension of the SM (MSSM)[3]. If there are SUSY particles (sparticles) with masses $10^2 \sim 10^3$ GeV, the reason why the mass of the Higgs particle is much smaller than the GUT scale is naturally understood. Moreover, the lightest SUSY particle (LSP) is a natural candidate for the dark matter (DM). We call such a kind of theory “natural SUSY”.

First, in this paper, we propose three sets of the SUSY parameters which are consistent with the experimental results of (i) the Higgs mass, (ii) the muon $g-2$, (iii) the DM abundance, (iv) $\text{Br}(b \rightarrow s\gamma)$, (v) $\text{Br}(B_s \rightarrow \mu^+\mu^-)$ and (vi) the direct search for the sparticles at the high energy colliders. Previous works often have only considered for either the DM abundance[4, 5, 6] or the muon $g-2$ [7, 8] constraints on the MSSM. We assume that both constraints are simultaneously significant. ATLAS collaboration[9] consider above all experimental constraints in the choice of the benchmark parameter sets. Differences of our approach from that of ATLAS collaboration is in the treatment of the uncertainty of the muon $g-2$. We used SuSpect2[10], SUSY-HIT[11] and micrOMEGAs[12] to calculate the MSSM predictions for (i) \sim (v).

The next purpose of our study is to calculate the 1-loop effects of sparticles in the processes $e^-e^+ \rightarrow \tau^-\tau^+$, $\bar{b}b$, $\bar{t}t$ at the International Linear Collider (ILC)[13] for selected parameter sets with using GRACE system for the MSSM calculations[14, 15]. We can expect the viable loop effects of even heavy sparticles with masses larger than the beam energy in the processes. We have confirmed that the numerical values of cross sections are consistent with those presented in the previous work[16].

This paper is organized as follows: In Section 2, we discuss the selection of the MSSM sets. In Section 3 we show the numerical results for cross sections of the production processes at the ILC. In Section 4, we give a summary and conclusions.

2 Selection of the MSSM parameter sets

2.1 The muon $g-2$ anomaly

There is a 3.5σ deviation between the SM prediction a_μ^{SM} and the experimental value a_μ^{exp} of the muon magnetic moment $g-2$ [17], where $a_\mu = (g - 2)/2$,

$$a_\mu^{exp} = (1165920.91 \pm 0.54 \pm 0.33) \times 10^{-9}, \quad (1)$$

$$a_\mu^{SM} = (1165918.03 \pm 0.01 \pm 0.42 \pm 0.26) \times 10^{-9}. \quad (2)$$

If the deviation,

$$\Delta a_\mu = (2.88 \pm 0.63 \pm 0.49) \times 10^{-9} \quad (3)$$

comes from the MSSM contribution, it becomes a constraint on the MSSM parameters. We strictly consider the uncertainty of the SM prediction in eq.(2). On the other hand, the possible larger statistical error in the estimation of the higher order SM contributions are taken into account by ATLAS collaboration[9]. The analytic expressions for the MSSM contributions to the muon $g-2$ [18] are given by

$$a_\mu(\tilde{W} - \tilde{H}, \tilde{\nu}_\mu) = \frac{g^2}{8\pi^2} \frac{m_\mu^2 M_2 \mu \tan \beta}{m_{\tilde{\nu}}^4} F_a \left(\frac{M_2^2}{m_{\tilde{\nu}}^2}, \frac{\mu^2}{m_{\tilde{\nu}}^2} \right), \quad (4)$$

$$a_\mu(\tilde{B}, \tilde{\mu}_L - \tilde{\mu}_R) = \frac{g_Y^2}{8\pi^2} \frac{m_\mu^2 \mu \tan \beta}{M_1^3} F_b \left(\frac{m_{\tilde{\mu}_L}^2}{M_1^2}, \frac{m_{\tilde{\mu}_R}^2}{M_1^2} \right), \quad (5)$$

$$a_\mu(\tilde{W} - \tilde{H}, \tilde{\nu}_\mu) = \frac{g_Y^2}{16\pi^2} \frac{m_\mu^2 M_1 \mu \tan \beta}{m_{\tilde{\nu}}^4} F_b \left(\frac{M_1^2}{m_{\tilde{\mu}_L}^2}, \frac{\mu^2}{m_{\tilde{\mu}_L}^2} \right), \quad (6)$$

$$a_\mu(\tilde{W} - \tilde{H}, \tilde{\nu}_\mu) = \frac{g^2}{16\pi^2} \frac{m_\mu^2 M_2 \mu \tan \beta}{m_{\tilde{\nu}}^4} F_b \left(\frac{M_2^2}{m_{\tilde{\mu}_L}^2}, \frac{\mu^2}{m_{\tilde{\mu}_L}^2} \right), \quad (7)$$

$$a_\mu(\tilde{W} - \tilde{H}, \tilde{\nu}_\mu) = \frac{g_Y^2}{8\pi^2} \frac{m_\mu^2 M_1 \mu \tan \beta}{m_{\tilde{\mu}_R}^4} F_a \left(\frac{M_1^2}{m_{\tilde{\mu}_R}^2}, \frac{\mu^2}{m_{\tilde{\mu}_R}^2} \right), \quad (8)$$

where g and g_Y are the coupling constants of the SU(2) and U(1) gauge groups; $m_{\tilde{\nu}}$ and $m_{\tilde{\mu}}$ are the masses of the sneutrino($\tilde{\nu}$) and the smuon($\tilde{\mu}$), respectively; μ is the Higgsino mass parameter; $\tan \beta$ is the ratio of two Higgs vacuum expectation values; M_1 and M_2 are the bino and the wino masses, respectively. The functions $F_a(x, y)$ and $F_b(x, y)$ are defined as follows,

$$F_a(x, y) = -\frac{G_1(x) - G_1(y)}{x - y}, \quad F_b(x, y) = -\frac{G_2(x) - G_2(y)}{x - y}, \quad (9)$$

where

$$G_1(x) = \frac{1}{2(x-1)^3}((x-1)(x-3) + 2 \log x), \quad (10)$$

$$G_2(x) = \frac{1}{2(x-1)^3}((x-1)(x-1) + 2x \log x). \quad (11)$$

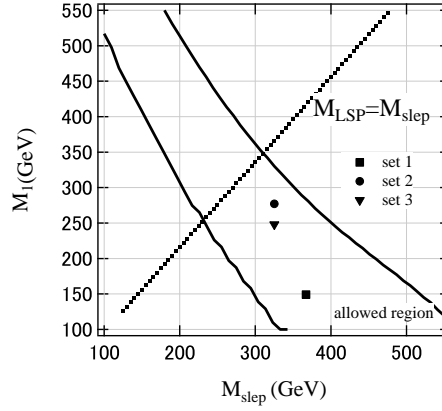


Figure 1: Allowed region from the muon $g-2$ constraint for $\tan \beta = 30$ and $\mu = 600\text{GeV}$. Dotted line corresponds to $M_{LSP} = M_{slep}$.

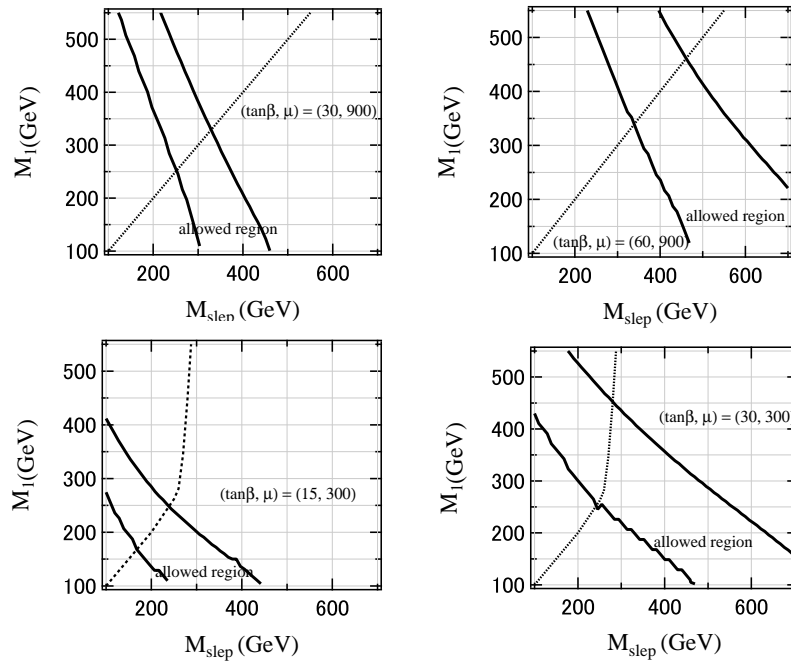


Figure 2: Dependences on $\tan \beta$ and μ of allowed regions by the muon $g-2$ constraint.

The allowed region from the muon $g-2$ constraint in (M_{slep}, M_1) plane for $\tan\beta = 30$ and $\mu = 600\text{GeV}$ is shown in Figure 1, where M_{slep} stands for $m_{\tilde{\nu}} = m_{\tilde{\mu}_L} = m_{\tilde{\mu}_R} + 5\text{GeV}$ in eqs.(4) \sim (8). The region between two solid lines is allowed. We also plot a line corresponds to $M_{LSP} = M_{slep}$. We should consider the region under the line in which the lightest neutralino $\tilde{\chi}_1^0$ can be the stable LSP and a candidate for the DM. For reference the points of three selected sets (Table 2, see Sec.2.5) are shown by markers.

It is important that the upper bounds of both M_1 and M_{slep} are roughly obtained for the fixed μ and $\tan\beta$. The dependences of allowed regions on μ and $\tan\beta$ are shown in Figure 2. While the regions are changed with μ and $\tan\beta$, we find that the rough upper limits of (M_{slep}, M_1) are $\sim (700, 450)\text{GeV}$. The muon $g-2$ is the dominant constraint in our selection of the parameter sets and provides credible experimental results which support “natural SUSY”.

2.2 Observed value of the Higgs mass

The measured mass of the Higgs boson is given by[1, 2]

$$m_h^{exp} = 125.7 \pm 0.4 \text{ GeV}. \quad (12)$$

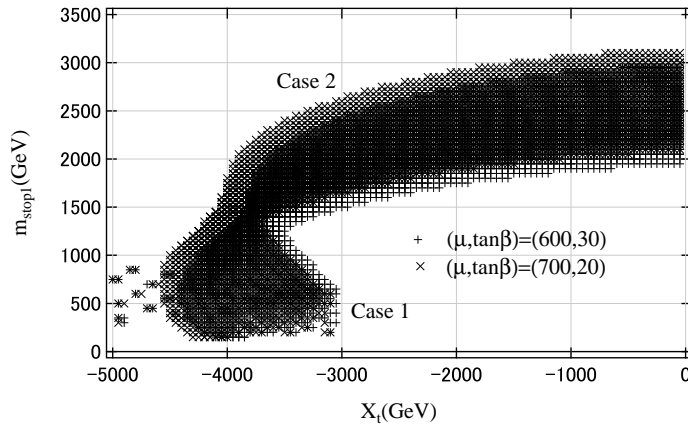


Figure 3: Contours on the $(X_t, m_{\tilde{t}_1})$ plane which are consistent with the observed mass of the Higgs boson for $(\mu, \tan\beta) = (600\text{GeV}, 30)$ and $(700\text{GeV}, 20)$. We take other MSSM parameters in set 1 (Table 2, see Sec.2.5).

We show the region which is consistent with the observed Higgs mass in $(X_t, m_{\tilde{t}_1})$ plane in Figure 3, where

$$X_t = \frac{m_{\tilde{t}_2}^2 - m_{\tilde{t}_1}^2}{m_t} \sin 2\theta_t = 2(A_t - \mu \cot\beta) \quad (13)$$

is the left-right mixing parameters of stops. A_t is a trilinear coupling which is one of the soft SUSY breaking parameters. In order to explain the Higgs mass in the MSSM, there are two potential cases: (Case 1) the lighter stop mass $m_{\tilde{t}_1} \lesssim 1.5\text{TeV}$ and $X_t = -(5 \sim 3)\text{TeV}$ or (Case 2) $m_{\tilde{t}_1} > 1.5\text{TeV}$ and $X_t \gtrsim -4\text{TeV}$. Note that the Cases 1 and 2 correspond to the light and the heavy stop scenario, respectively.

2.3 The DM abundance, $b \rightarrow s\gamma$ and $B_s \rightarrow \mu^+\mu^-$

A detail analyses of the fluctuation in the cosmic background radiation gives a severe constraint on the DM abundance[19]

$$\Omega h^2 = 0.1198 \pm 0.0026. \quad (14)$$

Naively, the higgsino-like LSP with a mass $\mathcal{O}(10^2)\text{GeV}$ can be a good candidate for the DM, because their abundance becomes $\mathcal{O}(10^{-1})$ [4]. However, it is difficult to meet these conditions given recent measurements of the Higgs mass and the branching ratios[20],

$$\text{Br}(B \rightarrow X_s\gamma) = (3.43 \pm 0.21 \pm 0.07) \times 10^{-4}, \quad (15)$$

$$\text{Br}(B_s \rightarrow \mu^+\mu^-) = (3 \pm 1) \times 10^{-9}. \quad (16)$$

For example, the A_t dependence of the $\text{Br}(b \rightarrow s\gamma)$ and m_h are shown in Figure 4.

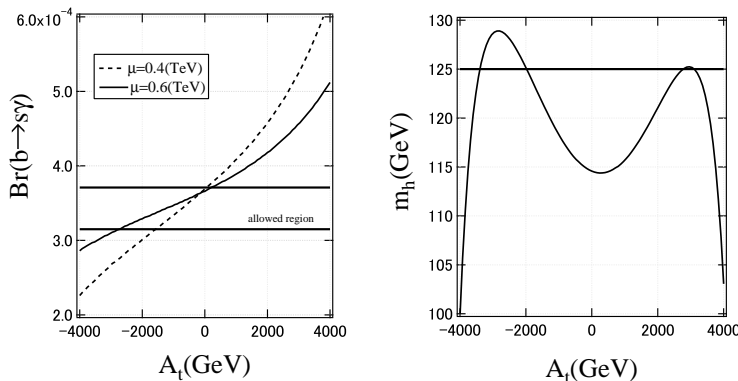


Figure 4: A_t dependence of $\text{Br}(b \rightarrow s\gamma)$ (left) and m_h (right). We take other MSSM parameters in set 1 (Table 2, see Sec.2.5).

We find that the allowed range eq.(15) for $\text{Br}(b \rightarrow s\gamma)$ and observed Higgs mass $m_h = 125\text{GeV}$ can achieve only for $A_t = -2\text{TeV}$ and $\mu = 0.6\text{TeV}$ in Fig.4. In general, we need $\mu \gtrsim 0.5\text{TeV}$ to meet both constraints. Here we recall the upper bound for the bino mass $M_1 \lesssim 0.45\text{TeV}$ and it must be smaller than the higgsino mass μ . Namely, the lightest neutralino $\tilde{\chi}_1^0$ should be almost bino with some wino and higgsino components. To meet the DM constraint eq.(14) with bino LSP, the co-annihilation should be occurred in addition to the simple annihilation processes. In the co-annihilation[21], the next lightest SUSY particle (NLSP) plays an important role. Here, we consider two cases, the NLSP is the lighter stop \tilde{t}_1 (stopCA) or the lighter stau $\tilde{\tau}_1$ (stauCA). The DM abundance depends sensitively on the mass degeneracy ΔM_{stop} and ΔM_{stau} , which are defined by

$$\Delta M_{stop} = \frac{m_{\tilde{t}_1} - m_{\tilde{\chi}_1^0}}{m_{\tilde{\chi}_1^0}}, \quad \Delta M_{stau} = \frac{m_{\tilde{\tau}_1} - m_{\tilde{\chi}_1^0}}{m_{\tilde{\chi}_1^0}}. \quad (17)$$

In Figure 5, we show the dependence of the DM abundance on these parameters. It is found that the desired value of the DM abundances are the sum of the simple annihilation $\tilde{\chi}_1^0\tilde{\chi}_1^0$ and the co-annihilation contributions $\tilde{t}_1\tilde{\chi}_1^0$, $\tilde{t}_1\tilde{t}_1$, $\tilde{\tau}_1\tilde{\chi}_1^0$ and $\tilde{\tau}_1\tilde{\tau}_1$.

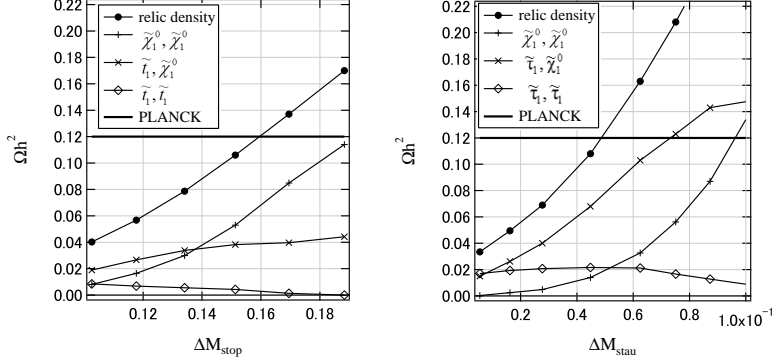


Figure 5: Dependence of the DM abundance on ΔM_{stop} ($m_{\tilde{t}_1}$) and on ΔM_{stau} ($m_{\tilde{\tau}_1}$) in left and right panel. The measured abundance by the PLANCK satellite is also shown. We take other MSSM parameters in set 1 and set 3 for right and left panel (Table 2, see Sec.2.5).

2.4 The searches for sparticles at the LHC

Despite the systematic searches for the sparticles at the LHC, the evidence of the SUSY has not yet been reported. The lower limits on the masses of the sparticles have been updated. For example, the lower limits on the masses of the first- and second-generation squarks and gluino[22],

$$m_{\tilde{q}}, m_{\tilde{g}} \gtrsim 1.5\text{TeV} \quad (18)$$

have been obtained by the analyses of the events with the large missing transverse energies.

Given the renormalization group equations (RGE) for the mass parameters in the MSSM assuming the GUT, it is theoretically natural that the first- and second-generation squarks \tilde{q} ($q = u, d, c, s$) and the gluino \tilde{g} have larger masses than the sleptons \tilde{l} , the charginos $\tilde{\chi}^\pm$ and the neutralinos $\tilde{\chi}^0$ due to the strong interaction. The lower mass limits of the chargino1 and the neutralino2 are $m_{\tilde{\chi}_1^\pm, \tilde{\chi}_2^0} \gtrsim 700\text{GeV}$ for $m_{\tilde{\chi}_1^0} \lesssim 400\text{GeV}$, when both the chargino and the neutralino decay only into e (μ) through the selectron (smuon)[23]. However, if they also decay to τ through the stau, there is no limit on $m_{\tilde{\chi}_1^\pm, \tilde{\chi}_2^0}$ for $m_{\tilde{\chi}_1^0} \gtrsim 200\text{GeV}$.

The masses of the stop \tilde{t} and the sbottom \tilde{b} have different RGE evolution from the other squarks because of their large Yukawa interaction in addition to the strong and electroweak interaction. The Yukawa interaction yields a negative contribution to the RGE of the mass parameters; thus, it is theoretically expected that \tilde{t} and \tilde{b} are lighter than \tilde{q}, \tilde{g} . Moreover, since the top quark mass is much greater than the other quark masses, there is a possibility that the difference between $m_{\tilde{t}_1}$ and the LSP mass $m_{\tilde{\chi}_1^0}$ is smaller than m_t . In this case, the stop has various possible decay modes $\tilde{t}_1 \rightarrow b\tilde{\chi}_1^+$, $bW^+\tilde{\chi}_1^0$, $c\tilde{\chi}_1^0$, $bq\tilde{q}\tilde{\chi}_1^0$, $b\ell^+\nu\tilde{\chi}_1^0$, $u\tilde{\chi}_1^0$ depending on the MSSM parameters. The excluded regions of the direct-stop searches with using those complicated signals at ATLAS and CMS are combined in Figure 6[24, 25]. As the b -quark is not so heavy, the sbottom \tilde{b} can generally decay into b +LSP. So the search strategies for \tilde{b} is not so complicate compared to the stop and the limit $m_{\tilde{b}_1} \gtrsim 800\text{GeV}$ has been obtained[26].

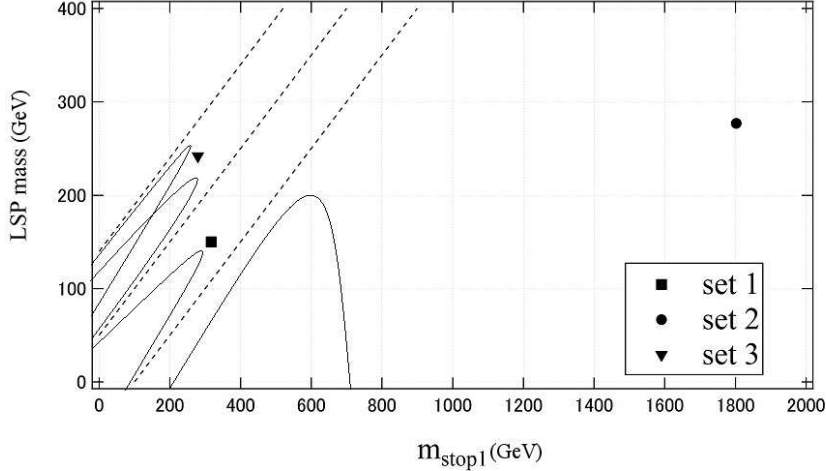


Figure 6: The excluded regions from the direct stop search at the LHC in $m_{\tilde{t}_1}-m_{\tilde{\chi}_1^0}$ space[24, 25].

2.5 Typical three MSSM parameter sets

Table 1: Typical MSSM parameter sets

	Case 1	Case 2
stauCA	set 1	set 2
stopCA	set 3	—

Based on discussion in the previous subsections, we consider a classification of the MSSM parameter sets into the four categories and have selected three sets 1 ~ 3 shown in Table 1. As has been mentioned in Sec.2.1, we strictly consider the muon $g-2$ constraint on the MSSM and adopt only “natural SUSY” sets with $m_{\tilde{\ell}, \tilde{\chi}^0, \tilde{\chi}^\pm} \lesssim 500\text{GeV}$. The two kinds of scenarios Cases 1 and 2 were introduced in Sec.2.2. We choose sets 1 and 3 for Case 1 with $m_{\tilde{t}_1} \lesssim 300\text{GeV}$. On the other hand, set 2 with $m_{\tilde{t}_1} \simeq 1.8\text{TeV}$ is an example of Case 2. The other two categories of scenarios were the types of the co-annihilation (or types of the NLSP) ; stauCA or stopCA. To achieve the DM abundance eq.(14), the mass degeneracy between $\tilde{\chi}_1^0$ and $\tilde{\tau}_1$ (\tilde{t}_1) plays an essential role in the sets 1 and 2 (set 3). Note that we have not chosen any set corresponded to Case 2 and StopCA. In this case the LSP becomes so heavy $m_{\tilde{t}_1} \sim m_{\tilde{\chi}_1^0} \gtrsim 1\text{TeV}$ that the muon $g-2$ constraint is not satisfied. In Tables 2 and 3 respectively important observables and the mass spectra for the three sets are shown.

Table 2: Important observables for three sets

	$m_h(\text{GeV})$	$\Delta a_\mu (\times 10^{-9})$	Ωh^2	$\text{Br}(b \rightarrow s\gamma) (\times 10^{-4})$	$\text{Br}(B_s \rightarrow \mu^+ \mu^-) (\times 10^{-9})$
set 1	125.71	2.30	0.121	3.02	3.96
set 2	125.74	2.11	0.120	3.11	3.65
set 3	125.97	2.24	0.120	3.01	4.00

set 1				set 2				set 3			
368.9	616.8			508.1	636.8			467.5	626.7		
$\tilde{\chi}_1^0$	$\tilde{\chi}_2^0$	$\tilde{\chi}_3^0$	$\tilde{\chi}_4^0$	$\tilde{\chi}_1^0$	$\tilde{\chi}_2^0$	$\tilde{\chi}_3^0$	$\tilde{\chi}_4^0$	$\tilde{\chi}_1^0$	$\tilde{\chi}_2^0$	$\tilde{\chi}_3^0$	$\tilde{\chi}_4^0$
149.0	369.0	604.0	616.2	177.9	508.5	603.4	637.2	142.8	467.6	603.6	626.7
$\tilde{\ell}_1$	$\tilde{\ell}_2$	$\tilde{\nu}_\ell$		$\tilde{\ell}_1$	$\tilde{\ell}_2$	$\tilde{\nu}_\ell$		$\tilde{\ell}_1$	$\tilde{\ell}_2$	$\tilde{\nu}_\ell$	
362.5	367.9	359.6		317.8	323.3	313.8		322.8	328.3	318.9	
$\tilde{\tau}_1$	$\tilde{\tau}_2$	$\tilde{\nu}_\tau$		$\tilde{\tau}_1$	$\tilde{\tau}_2$	$\tilde{\nu}_\tau$		$\tilde{\tau}_1$	$\tilde{\tau}_2$	$\tilde{\nu}_\tau$	
161.1	296.1	228.2		283.9	377.1	327.4		320.1	405.3	359.6	
\tilde{u}_1	\tilde{u}_2	\tilde{d}_1	\tilde{d}_2	\tilde{u}_1	\tilde{u}_2	\tilde{d}_1	\tilde{d}_2	\tilde{u}_1	\tilde{u}_2	\tilde{d}_1	\tilde{d}_2
1720	1739	1740	1741	1720	1739	1740	1741	1720	1739	1740	1741
\tilde{t}_1	\tilde{t}_2	\tilde{b}_1	\tilde{b}_2	\tilde{t}_1	\tilde{t}_2	\tilde{b}_1	\tilde{b}_2	\tilde{t}_1	\tilde{t}_2	\tilde{b}_1	\tilde{b}_2
317.0	2078	800.0	2061	1802	2244	1998	2062	189.6	2078	800.0	2061
θ_τ	θ_b	θ_t		θ_τ	θ_b	θ_t		θ_τ	θ_b	θ_t	
0.8071	1.557	1.456		0.8150	1.376	0.8533		0.8175	1.557	1.456	
M_1	M_2	M_3		M_1	M_2	M_3		M_1	M_2	M_3	
150.0	380.0	1500		280.0	540.0	1500		244.5	489.0	2000	
$\mu=600, \tan\beta=30$				$\mu=600, \tan\beta=30$				$\mu=600, \tan\beta=30$			

Main decay modes of the major particles are shown in Table 4. Note that the three sets are distinguished by the decay modes of the lighter stop. In set 1, \tilde{t}_1 mainly decays into $bW\tilde{\chi}_1^0$ because the mass difference between the \tilde{t} and $\tilde{\chi}_1^0$ is greater than m_W . In set 2, \tilde{t}_1 can decay into the $t\tilde{g}$ since $m_{\tilde{t}_1}$ is large enough. In set 3, \tilde{t}_1 can only decay into $c\tilde{\chi}_1^0$ because of small mass difference $(m_{\tilde{t}_1} - m_{\tilde{\chi}_1^0}) \sim 35\text{GeV}$. The main decay modes of \tilde{b}_1 , $\tilde{\chi}_1^\pm$ and $\tilde{\chi}_2^0$ are also different for the three sets. On the other hand, the gluino \tilde{g} signals can be used to distinguish the light and heavy stop scenarios.

Table 4: Main decay modes of the major MSSM particles.

	\tilde{t}_1	\tilde{b}_1	\tilde{g}	$\tilde{\chi}_1^+$	$\tilde{\chi}_2^0$	$\tilde{\ell}_{1,2}$
set 1	$bW\tilde{\chi}_1^0$	$b\tilde{\chi}_1^0, b\tilde{\chi}_3^0$	$t\tilde{t}_1, b\tilde{b}_1$	$\tau^+\tilde{\nu}_\tau, \nu_\tau\tilde{\tau}_1^+$	$\tau\tilde{\tau}_1, \bar{\nu}_\tau\tilde{\nu}_\tau$	$l\tilde{\chi}_1^0$
set 2	$t\tilde{g}, b\tilde{\chi}_1^+$	$b\tilde{g}$	$q\bar{q}\tilde{\chi}_1^0, q\bar{q}\tilde{\chi}_1^\pm$	$\ell^+\tilde{\nu}_\tau, \tau^+\tilde{\nu}_\tau$	$\ell\tilde{\ell}_2, \tau\tilde{\tau}_1, \nu\tilde{\nu}$	$l\tilde{\chi}_1^0$
set 3	$c\tilde{\chi}_1^0$	$b\tilde{\chi}_1^0, t\tilde{\chi}_1^-$	$t\tilde{t}_1, b\tilde{b}_1$	$b\tilde{t}_1, \ell^+\tilde{\nu}_\ell$	$t\tilde{t}_1$	$l\tilde{\chi}_1^0$

3 Numerical results for the $e^-e^+ \rightarrow \tau^-\tau^+, t\bar{t}, b\bar{b}$

3.1 The GRACE system and the calculation schemes

There are more than twice as many different types of particles in the MSSM as those in the SM ; therefore, there are various possible sparticle production processes in the collider experiments. Large number of generated Feynman diagrams causes the large number of calculations of the cross section of each production process. Accurate theoretical prediction requires an automated system to manage such large scale computation. GRACE system for the MSSM calculations[14, 15] has been developed in the KEK group (the Minami-tateya group) to meet the requirement. Measurements of the cross section will be possible in high precision at the ILC. Theoretical predictions to be compared with such high accuracy data, calculated in the physics of SUSY, are necessary to analyze the experimental data. The GRACE system uses a renormalization prescription that impose mass shell conditions on as many particles as possible, while maintaining the gauge symmetry by setting the renormalization conditions appropriately[15]. For the SM, the usual 't Hooft linear gauge condition is generalised to a more general non-linear gauge (NLG) that involves five extra parameters[27, 28]. We extend it to the MSSM formalism by adding the SUSY interactions with seven NLG parameters[15, 29]. We can check the consistency of the gauge symmetry by verifying the independence of the physical results on the NLG parameters.

We ascertain whether the results of the automatic calculation are reliable by carrying out the following checks:

- Electroweak(ELWK) non-linear gauge invariance check (NLG check)
- Cancellation check of ultraviolet divergence (UV check)
- Cancellation check of infrared divergence (IR check)
- Cut-off energy independence check (k_c check)

Actually, we calculate the 1-loop differential cross sections (distributions) separately,

$$d\sigma_{L\&S}^{M,G}(k_c) \equiv d\sigma_{\text{virtual}}^{M,G} + d\sigma_{\text{soft}}^G, \quad (19)$$

where M= (SM or MSSM) and G= (ELWK or QCD). The loop and the counter term contribution $d\sigma_{\text{virtual}}^{M,G}$ should be gauge invariant and the UV finite but IR divergent. We regularize the IR divergence by the fictitious photon (or gluon) mass λ , so both $d\sigma_{\text{virtual}}^{M,G}$ and the soft photon (or gluon) contribution $d\sigma_{\text{soft}}^G$ are λ dependent. The λ dependence is canceled in $d\sigma_{L\&S}^{M,G}$. Finally, the k_c independent 1-loop physical cross sections can be obtained by

$$d\sigma_{\text{1loop}}^{M,G} \equiv d\sigma_{\text{tree}} + d\sigma_{L\&S}^{M,G}(k_c) + \iint_{k_c} \frac{d\sigma_{\text{hard}}^G}{d\Omega dk} d\Omega dk, \quad (20)$$

where k and Ω are the energy and the solid angle of the photon (or gluon). Strictly, the tree level $d\sigma_{\text{tree}}$, the soft $d\sigma_{\text{soft}}^G$ and the hard photon (gluon) $d\sigma_{\text{hard}}^G$ contributions are different for the SM and the MSSM because their Higgs contributions are not identical.

However, those contributions are numerically negligible at least in the present processes $e^-e^+ \rightarrow f\bar{f}$, so we omitted the suffix M from them. We should note that the integration with possible numerical errors must be needed in the estimation of $d\sigma_{1\text{loop}}^{\text{M,G}}$. To verify the signature of existence of the new physics, one should use the quantity without uncertainty coming from the numerical integration. Thus, we define the ratio of the differential cross sections[16].

$$\delta_{\text{susy}}^{\text{G}} \equiv \frac{d\sigma_{1\text{loop}}^{\text{MSSM,G}} - d\sigma_{1\text{loop}}^{\text{SM,G}}}{d\sigma_{\text{tree}}} \quad (21)$$

We can accurately estimate the 1-loop MSSM effects because the hard photon (or gluon) contributions are canceled in the calculation of $\delta_{\text{susy}}^{\text{G}}$. Finally, we define the correction ratio of the sum of the ELWK and QCD contributions,

$$\delta_{\text{susy}} \equiv \delta_{\text{susy}}^{\text{ELWK}} + \delta_{\text{susy}}^{\text{QCD}}. \quad (22)$$

3.2 Selection of the beam energies

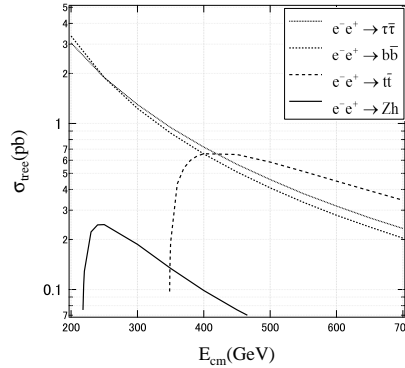


Figure 7: E_{cm} dependence of the tree-level total cross section for $e^-e^+ \rightarrow \tau^-\tau^+, b\bar{b}, t\bar{t}$ and Zh .

We show the center of mass energy (E_{cm}) dependence of the tree-level total cross sections for $e^-e^+ \rightarrow \tau^-\tau^+, b\bar{b}, t\bar{t}$ and Zh in Figure 7. One of the main purpose of the ILC project is the detail investigation of properties of the Higgs particle with many Higgs events; this will be realized at $E_{cm} = 250$ GeV, which is almost the peak energy for $e^-e^+ \rightarrow Zh$. So, first we choose to investigate the SUSY 1-loop effects in $e^-e^+ \rightarrow \tau^-\tau^+, b\bar{b}$ at this value of E_{cm} . The $t\bar{t}$ cross section rises at $E_{cm} \simeq 350$ GeV and has its peak at ~ 400 GeV. While we can expect large cross section at the energy region, the theoretical large uncertainty of perturbative QCD calculation will be expected. So we choose the second focused $E_{cm} = 500$ GeV for calculation of $e^-e^+ \rightarrow \tau^-\tau^+, b\bar{b}, t\bar{t}$.

We find that the tree level total cross section $\sigma(e^-e^+ \rightarrow \tau^-\tau^+, b\bar{b}) \simeq (2.0, 0.5)\text{pb}$ for $E_{cm} = (250, 500)\text{GeV}$ in Fig. 7. In estimation of the statistical errors for the cross sections and correction ratios, we assume the integrated luminosities $L = (250, 500) \text{fb}^{-1}$ for $E_{cm} = (250, 500)\text{GeV}$, which are planned values at the ILC project[13]. Therefore, for example, the statistical error for the total cross section is $\Delta \simeq (0.15, 0.20)\%$ for $E_{cm} = (250, 500)\text{GeV}$. As for the physical distributions, estimated errors depend on the number of bins (N_{bin}). In the following calculation, we take $N_{\text{bin}} = 20$.

3.3 $e^-e^+ \rightarrow \tau^-\tau^+, b\bar{b}$ at $E_{cm} = 250$ GeV

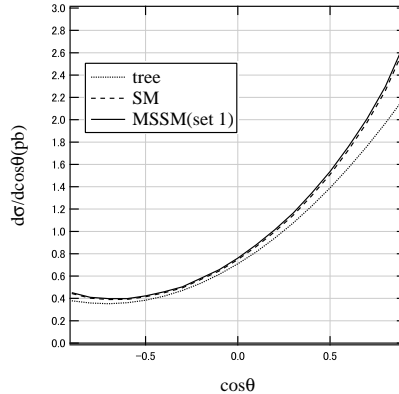


Figure 8: 1-loop corrected angular distribution of τ^- in $e^-e^+ \rightarrow \tau^-\tau^+$ at $E_{cm} = 250$ GeV. Dotted, dashed and solid line respectively corresponds to the tree, SM 1-loop and MSSM (set 1) 1-loop level cross section.

We show the ELWK 1-loop corrected angular distribution of τ^- in $e^-e^+ \rightarrow \tau^-\tau^+$ at $E_{cm} = 250$ GeV in Figure 8. The 1-loop correction is larger for the forward and the backward regions (e.g. $\sim +20\%$ for $|\cos\theta| \simeq 0.9$) than the central region (e.g. $\sim +6\%$ for $\cos\theta \simeq 0$). Measurements are expected to be accurate to within a few percent at the ILC, therefore, we must consider the ELWK 1-loop correction in the theoretical prediction of the physical distributions. Since the main contribution of the ELWK correction is dominated by the SM contribution, the difference between the MSSM and the SM plots is small. Moreover, the results of set 1 are only plotted because the difference among parameter sets is not so apparent in the angular distributions.

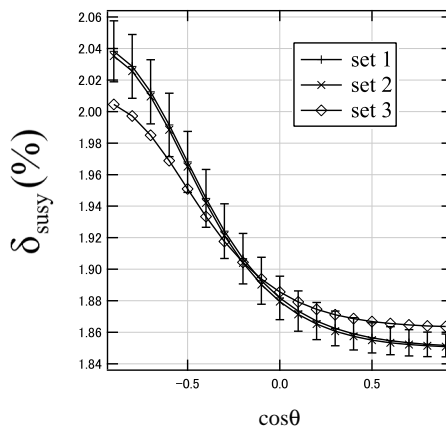


Figure 9: Correction ratios for three parameter sets in $e^-e^+ \rightarrow \tau^-\tau^+$ at $E_{cm} = 250$ GeV.

The values of $\delta_{\text{susy}}^{\text{ELWK}}$ for each parameter set are shown in Figure 9. For the three sets, $\delta_{\text{susy}}^{\text{ELWK}}$ is $\sim +2\%$ and the statistical error for each bin is about $\pm 1\%$ over the entire region. If measurements were to be carried out within the 2% accuracy at the ILC, the deviation from the SM prediction for the three sets would be statistically verifiable. On the other hand, however, discrimination among the three parameter sets is substantially difficult.

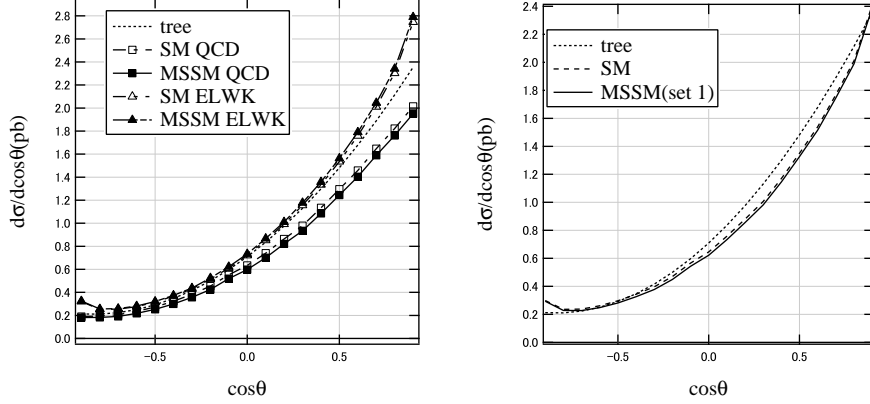


Figure 10: 1-loop corrected angular distributions of b in $e^-e^+ \rightarrow b\bar{b}$ at $E_{cm} = 250$ GeV. The left figure shows a detail of the QCD and ELWK corrections separately and the right panel is the sum of the QCD and ELWK corrections.

We show the ELWK and QCD 1-loop corrected angular distributions of the b -quark in $e^-e^+ \rightarrow b\bar{b}$ in Figure 10. The ELWK and QCD correction is respectively about +15% and -20% around $\cos\theta \simeq 0.9$, for example. The positive ELWK and the negative QCD contributions are canceled each other over the entire region, so the magnitude of the MSSM 1-loop correction is about $0.0 \pm 5.0\%$. Similar to the τ pair production, the correction is dominated by the SM contribution.

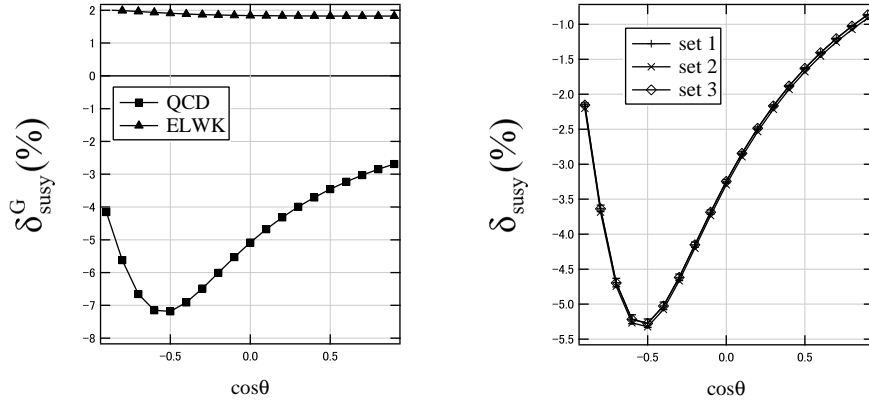


Figure 11: The correction ratio of QCD and ELWK for $e^-e^+ \rightarrow b\bar{b}$ at $E_{cm} = 250$ GeV. In the left, 1-loop QCD and ELWK contributions are shown separately, and in the right, the total corrections are shown.

The values of δ_{susy}^G are shown in Figure 11. In the left panel, we find that the ELWK correction is about +2% similar to $\tau^-\tau^+$ process and, on the other hand, the QCD correction is $(-7.0 \sim -2.5)\%$. As a total, $\delta_{\text{susy}} \simeq (-5.0 \sim -0.5)\%$ for the three parameter sets. Since the statistical error for each bin is $\pm(0.5 \sim 1.0)\%$ over the entire region, the deviation from the SM in all parameter sets would be statistically verifiable with the expected accuracy of the ILC experiments. We emphasize that evidence of the MSSM might be confirmed during the early stages of experiments at the ILC, manifested as a 5% difference in bottom-pair production between the SM and the MSSM.

3.4 $e^-e^+ \rightarrow \tau^-\tau^+, b\bar{b}$ and $t\bar{t}$ at $E_{cm} = 500$ GeV.

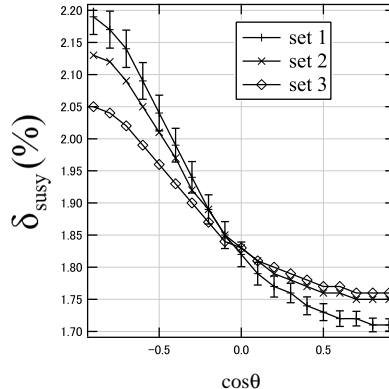


Figure 12: Correction ratio of the MSSM for the SM predictions at $E_{cm} = 500$ GeV for $e^+e^- \rightarrow \tau^-\tau^+$.

The values of $\delta_{\text{susy}}^{\text{ELWK}}$ for $e^-e^+ \rightarrow \tau^-\tau^+$ of the three parameter sets are shown in Figure 12. It is significant that the difference among parameter sets is larger than the statistical error in the tau-pair production. For example, the difference between set 1 and set 3 is as much as 0.15% in the backward direction ($\cos\theta \simeq -0.9$). While we are not able to conclude this simply without taking into account the experimental systematic error, there is a possibility for us to distinguish the sets from one another at $E_{cm} = 500$ GeV.

We have not shown any plot for $b\bar{b}$ production at $E_{cm} = 500$ GeV because results can be easily expected by those at $E_{cm} = 250$ GeV. The angular dependences of $d\sigma/d\cos\theta$ and δ_{susy} are almost the same to Figs. 10 and 11, respectively. Of course, the values of $d\sigma/d\cos\theta$ are about uniformly quarter of those at $E_{cm} = 250$ GeV.

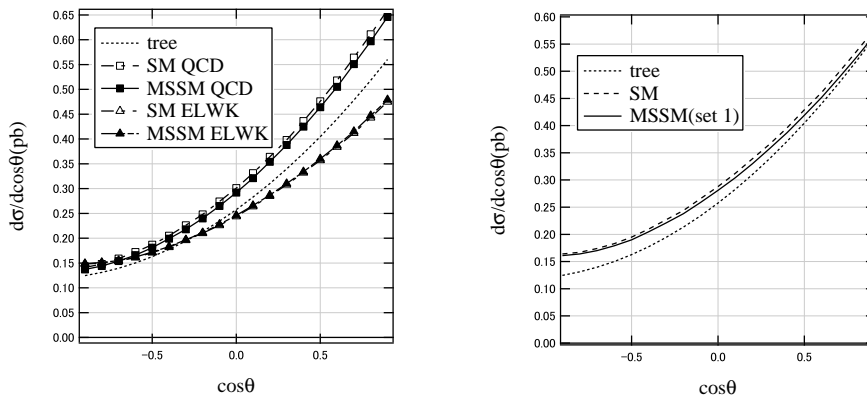


Figure 13: One-loop corrected angular distribution for $e^-e^+ \rightarrow t\bar{t}$ at $E_{cm} = 500$ GeV. The left figure shows a detail of the QCD and ELWK corrections separately and the right panel is the sum of the QCD and ELWK corrections.

Finally, we show the 1-loop corrected angular distributions of the top quark in $e^-e^+ \rightarrow t\bar{t}$ in Figure 13. The QCD and the ELWK corrections are separately shown in the left panel. Both the QCD and the ELWK corrections are almost the same value ($0 \sim +10\%$) in the backward region. In the forward region, on the other hand, the QCD and the ELWK

correction is (+10 ~ +20%) and (-15 ~ 0%), respectively. Two types of corrections are canceled in the forward and added to become up to +30% in the backward region.

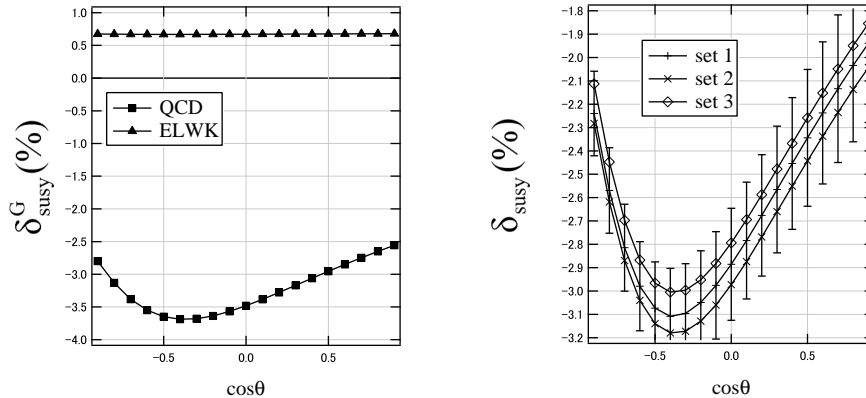


Figure 14: The correction ratio of QCD and ELWK for $e^-e^+ \rightarrow t\bar{t}$ at $E_{cm} = 500$ GeV. In the left, 1-loop QCD and ELWK contributions are shown separately, and in the right, the total corrections are shown.

The values of δ_{susy}^G for $t\bar{t}$ production are shown in Figure 14. In the left panel, we find that the ELWK correction is about +0.7% and, on the other hand, the QCD correction is (-3.7 ~ -2.5)%. As a total, $\delta_{\text{susy}} \simeq (-3.2 \sim -1.9)\%$ for the three parameter sets and the statistical error for each bin is $\pm(0.5 \sim 1.0)\%$ over the entire region. If measurements were to be carried out within the 3% accuracy at the ILC, the deviation from the SM prediction for three sets would be statistically verifiable.

4 Summary and conclusions

We have proposed three possible types of categories for the MSSM scenarios which are consistent with the experimental results of the Higgs mass, the muon $g-2$, the DM abundance, $\text{Br}(b \rightarrow s\gamma)$, $\text{Br}(B_s \rightarrow \mu^+\mu^-)$ and the direct search for the sparticles at the high energy colliders. For selected three typical parameter sets, 1-loop level cross sections of $e^-e^+ \rightarrow \tau^-\tau^+$, $b\bar{b}$, $t\bar{t}$ at $E_{cm} = 250$ and 500 GeV have been calculated by using GRACE/SUSY-loop. If we assume the experimental accuracy at the ILC project, we will be able to verify the effects of virtual sparticles in the selected parameter sets through the detail measurements of angular distributions of the third generation fermion productions. In particular, the effect of the MSSM for $b\bar{b}$ production at $E_{cm} = 250\text{GeV}$ will be expected to become about 5% in the observable δ_{susy} . As for the discrimination of the parameter sets, $\tau^-\tau^+$ production at $E_{cm} = 500\text{GeV}$ seems to be the most promising. We expect the discovery of the simple “natural SUSY” scenarios at the LHC, for example $m_{\tilde{q},\tilde{g}} \lesssim 2\text{TeV}$ (e.g. set 2). However, other scenarios are possible, for example, the case where $m_{\tilde{t}} \sim m_{\tilde{\chi}_1^0}$ (set 3) or the case where $m_{\tilde{\tau}} \sim m_{\tilde{\chi}_1^0}$ (set 1), and they might be difficult to be explored at the LHC. We would confirm such scenarios if the present processes were to be examined in detail at the ILC.

References

- [1] ATLAS Collaboration, Phys. Lett., **B716**, 1 (2012).
- [2] CMS Collaboration, Phys. Lett., **B716**, 30 (2012).
- [3] S. P. Martin, Adv. Ser. Direct. High Energy Phys. **18**, 1 (1998), hep-ph/9709356v7 (2016).
- [4] A. Ibarra, A. Pierce, N. R. Shah, and S. Vogl, Phys. Rev. D, **91**, 095018 (2015).
- [5] J. Ellis, K. A. Olive, and J. Zheng, Eur. Phys. J., **C74**, 2947 (2014).
- [6] M. Endo, K. Hamaguchi, S. Iwamoto, T. Kitahara, and T. Moroi, Phys. Lett., **B728**, 274 (2014).
- [7] B. P. Padley, K. Sinha, and K. Wang, Phys. Rev. D, **92**, 055025 (2015).
- [8] K. Hamaguchi and K. Ishikawa, Phys. Rev. D, **93**, 055009 (2016).
- [9] ATLAS Collaboration, JHEP, **10**, 134 (2015).
- [10] A. Djouadi, J.-L. Kneur, and G. Moultaka, Comput. Phys. Commun., **176**, 426 (2007).
- [11] A. Djouadi, M. M. Muhlleitner, and M. Spira, Acta Phys. Polon., **B38**, 635 (2007).
- [12] G. Bélanger, F. Boudjema, A. Pukhov, and A. Semenov, Comput. Phys. Commun., **149**, 103 (2002).
- [13] H. Baer, T. Barklow, K. Fujii, Y. Gao, A. Hoang, S. Kanemura, J. List, H. E. Logan, A. Nomerotski, M. Perelstein, et al. (2013), arXiv:1306.6352.
- [14] J. Fujimoto, T. Ishikawa, M. Jimbo, T. Kaneko, K. Kato, S. Kawabata, T. Kon, M. Kuroda, Y. Kurihara, Y. Shimizu, and H. Tanaka, Comput. Phys. Commun., **153**, 106 (2003).
- [15] J. Fujimoto, T. Ishikawa, Y. Kurihara, M. Jimbo, T. Kon, and M. Kuroda, Phys. Rev. D, **75**, 113002 (2007).
- [16] W. Hollik and C. Schappacher, Nucl. Phys., **B545**, 98–140 (1999).
- [17] A. Hoecker and W. J. Marciano, The Muon Anomalous Magnetic Moment, in Particle Data Group, Chin. Phys., **C38**, 090001 (2014); p.649 (updated August 2013), references therein.
- [18] G. C. Cho, K. Hagiwara, Y. Matsumoto, and D. Nomura, JHEP, **11**, 068 (2011).
- [19] Planck Collaboration (2015), arXiv:1502.01582.
- [20] T. Becher and M. Neubert, Phys. Rev. Lett., **98**, 022003 (2007).

- [21] K. A. Olive, PoS, **PLANCK2015**, 093 (2015).
- [22] ATLAS Collaboration, JHEP, **09**, 176 (2014).
- [23] ATLAS Collaboration, JHEP, **04**, 169 (2014).
- [24] ATLAS Collaboration, Phys. Rev. D, **90**, 052008 (2014).
- [25] The CMS Collaboration, Eur. Phys. J. C, **73**, 2677 (2013).
- [26] ATLAS Collaboration, JHEP, **10**, 189 (2013).
- [27] F. Boudjema and E. Chopin, Z. Phys., **73**, 85 (1997).
- [28] G. Bélanger, F. Boudjema, J. Fujimoto, T. Ishikawa, T. Kaneko, K. Kato, and Y. Shimizu, Nucl. Phys. Proc. Suppl., **116**, 353 (2003).
- [29] N. Baro and F. Boudjema, Phys. Rev. D, **80**, 076010 (2009).